



HAL
open science

A numerical analysis of the short open load calibration robustness for capacitance measurements in scanning microwave microscopy

Damien Richert, Damien Deleruyelle, José Morán-Meza, Khaled Kaja, Almazbek Imanaliev, Johannes Hoffmann, Brice Gautier, François Piquemal

► To cite this version:

Damien Richert, Damien Deleruyelle, José Morán-Meza, Khaled Kaja, Almazbek Imanaliev, et al.. A numerical analysis of the short open load calibration robustness for capacitance measurements in scanning microwave microscopy. *Measurement Science and Technology*, 2024, 36 (1), pp.015013. 10.1088/1361-6501/ad7e3b . hal-04814141

HAL Id: hal-04814141

<https://hal.science/hal-04814141v1>

Submitted on 13 Jan 2025

HAL is a multi-disciplinary open access archive for the deposit and dissemination of scientific research documents, whether they are published or not. The documents may come from teaching and research institutions in France or abroad, or from public or private research centers.

L'archive ouverte pluridisciplinaire **HAL**, est destinée au dépôt et à la diffusion de documents scientifiques de niveau recherche, publiés ou non, émanant des établissements d'enseignement et de recherche français ou étrangers, des laboratoires publics ou privés.



Distributed under a Creative Commons Attribution 4.0 International License

PAPER • OPEN ACCESS

A numerical analysis of the short open load calibration robustness for capacitance measurements in scanning microwave microscopy

To cite this article: Damien Richert *et al* 2025 *Meas. Sci. Technol.* **36** 015013

View the [article online](#) for updates and enhancements.

You may also like

- [In-flight pixel degradation of the Sentinel 5 Precursor TROPOMI-SWIR HgCdTe detector](#)
Tim A van Kempen, Marina Lobanova, Richard van Hees et al.
- [A comprehensive bearing prognosis framework based on piecewise function stacking convolution auto-encoder and XGBoost algorithm](#)
Huashan Chi, Yuanyu Wei, Bo Yuan et al.
- [Measurement method of flexible component pose based on discrete motion actuators](#)
Zhengtao Wu, Shuanggao Li, Wenmin Chu et al.



UNITED THROUGH SCIENCE & TECHNOLOGY

 **The Electrochemical Society**
Advancing solid state & electrochemical science & technology



**248th
ECS Meeting**
Chicago, IL
October 12-16, 2025
Hilton Chicago

**Science +
Technology +
YOU!**

**SUBMIT
ABSTRACTS by
March 28, 2025**

SUBMIT NOW

A numerical analysis of the short open load calibration robustness for capacitance measurements in scanning microwave microscopy

Damien Richert¹ , Damien Deleruyelle^{2,3}, José A Morán-Meza¹, Khaled Kaja¹, Almazbek Imanaliev¹, Johannes Hoffmann⁴, Brice Gautier^{2,3} and François Piquemal^{1,*} 

¹ Laboratoire National de métrologie et d'Essais (LNE), Trappes Cedex, France

² Institut National des Sciences Appliquées de Lyon (INSA), Villeurbanne, France

³ Institut des Nanotechnologies de Lyon (INL), Villeurbanne, France

⁴ Federal Institute of Metrology METAS, Bern-Wabern, Switzerland

E-mail: francois.piquemal@lne.fr

Received 26 January 2024, revised 29 August 2024

Accepted for publication 23 September 2024

Published 18 October 2024



CrossMark

Abstract

Numerous experimental parameters affect the accuracy of impedance measurements in scanning microwave microscopy (SMM). Investigating their effects on the measured values is particularly challenging. Here, we present the development of a fully-numerical finite element method-based simulation of the actual SMM measurements. We demonstrate the application of a self-calibration procedure for the simulated SMM measurements with a maximal deviation of $\pm 0.8\%$ relative to reference capacitances determined via an electrostatic finite element model. Furthermore, we demonstrate the possibility of assessing water meniscus-induced effects on the simulated SMM measurements. Typically, water meniscus impacts the calibration by a 0.4% relative deviation, in accordance with previously reported empiric data. Our findings are expected to promote access to a deeper understanding of nanoscale capacitance measurements in SMM.

Keywords: scanning microwave microscopy, finite element analysis, tip apex geometry, self-calibration, Maxwell equation

1. Introduction

As new nanomaterials and nanostructures are being ubiquitously incorporated into the novel architectures of nanoelectronic components at unprecedented small scales, the need

for reliable nanoscale characterization methods has become increasingly important. To align with the functionality of the novel devices and components, measuring the nanoelectrical properties of materials under various electromagnetic and environmental conditions constitutes a major requirement for enabling the identification of adequate fabrication processes. Scanning microwave microscopy (SMM) is a pioneering method for measuring the electromagnetic properties of materials at the nanoscale in the microwave (MW) domain [1, 2]. By coupling an atomic force microscope (AFM) to a vector network analyzer (VNA), SMM enables the local measurement of impedances, leading to the characterization of properties such as permittivity, dielectric loss, and conductivity. As

* Author to whom any correspondence should be addressed.



Original content from this work may be used under the terms of the [Creative Commons Attribution 4.0 licence](https://creativecommons.org/licenses/by/4.0/). Any further distribution of this work must maintain attribution to the author(s) and the title of the work, journal citation and DOI.

all measurement techniques based on VNA, the SMM needs to be calibrated before performing any measurement [3].

Despite the demonstrated capability of SMM in measuring the dielectric properties with very low uncertainty levels at a few percents [4, 5], the measurement's sensitivity to local changes in the experimental conditions and environment constitutes a major challenge for quantitative results. SMM operates in contact mode and the probe on the sample produces mainly an electric field which penetrates into the sample. At radiofrequencies (RF), the tip-sample system is exceptionally prone to all sorts of capacitive couplings, increasing the complexity of the interpretation of result. Furthermore, the contributions from stray capacitances induced by the probe's and sample's geometries may have a significant impact on the measurement. Identifying and decoupling the aforementioned effects is particularly challenging under experimental conditions.

We present the development of a digital-twin environment to reproduce the experimental measurements using finite element method (FEM)-based simulations. Although previously reported studies explained behavior of charges in semiconductors under an SMM tip [6, 7], our goal here is to build a comprehensive digital environment enabling the simulation of all possible experimental and environmental conditions affecting the electrical measurements in SMM. While this does not include comparisons between measurements and models for the capacitances used for calibration, it allows us to study effects such as the water meniscus which are very difficult to study experimentally. By tweaking the entire tip-sample geometry, we show that our approach offers the means to separate the contributions of all factors altering the measurement of the true sample impedance. More importantly, we demonstrate that our digital-twin-based method reproduces the SMM calibration procedures, which creates a self-calibration approach for quantitative estimation of impedance measurements errors. Early results of this work have already been the subject of a previous publication [8]. Since then, significant progress has been made in the modification performance reducing the error occurring in self-calibration of the instrument from $\pm 6\%$ to $\pm 0.8\%$. This progress made possible the study of factors such as water meniscus on the instrument calibration.

2. The need for calibration

2.1. Calibration procedure

When SMM measurement data are acquired, the goal is typically to measure the local impedance of the sample (Z_S). This is done by converting the reflection coefficient (S_{11}) into Z_S using equation 1,

$$S_{11} = \frac{Z_S - Z_0}{Z_S + Z_0}, \quad (1)$$

where Z_0 is the reference impedance (50Ω). Nevertheless, this relation is only true at the reference plane of the VNA. A schematic of a SMM experiment is shown in figure 1.

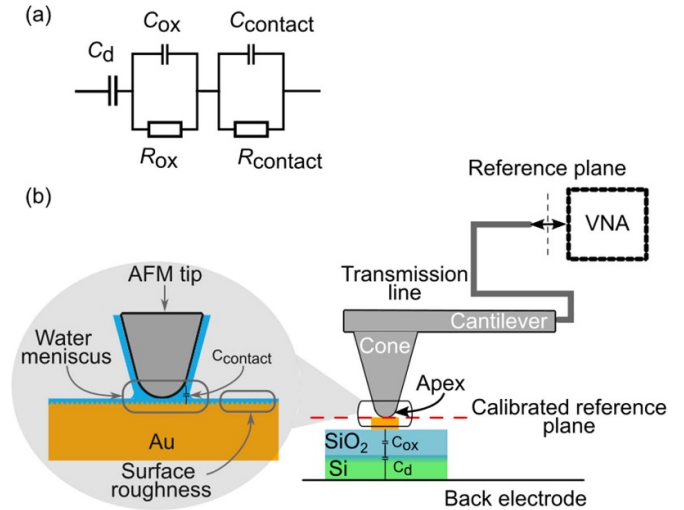


Figure 1. (a): equivalent circuit (b): schematic of the RF transmission line connected to the apex of the AFM probe. The orange continuous line on top of the cantilever is the electrical contact connecting the AFM tip to the RF signal. Zoom-in: tip-sample interface.

The equivalent circuit between the AFM apex and the back electrode is shown in figure 1(a) where C_d is the depletion capacitance in the semiconductor substrate, C_{ox} and R_{ox} are the capacitance and resistance of the dielectric layer, and $C_{contact}$ and $R_{contact}$ the capacitance and resistance of the tip-sample interface. Those parasitic impedances and the transmission line (figure 1(b)) create a difference in the S_{11} measured at the tip-sample interface (red dashed line) and at the reference plane of the VNA (black dashed line).

To access the S_{11} associated with the sample impedance, the reference plane has to be relocated at the interface tip-sample. This reference adjustment has been done in previous works [1, 4] by applying a modified Short Open Load calibration (mSOL) method on the SMM measurement using a capacitance calibration standards (figure 2). The signal S_{11} corrected by the mSOL method is given by

$$S_{11} = \frac{S_{11,m} - e_{00}}{e_{01} + e_{11}(S_{11,m} - e_{00})}, \quad (2)$$

where e_{ij} are the error parameters, S_{11} and $S_{11,m}$ are the reflection coefficients at the tip-sample interface and at the reference plane of the VNA respectively. This calibration procedure compensates for the loss and reflection occurring in the transmission line between the VNA and the apex of the tip [9]. To refine the uncertainty associated with the calibrated impedance measurement in SMM, it is of prime importance to assess the impact of environmental parameters on the propagation of the MW signal. In the following sections, we present a numerical model accounting for the tip-sample contact, the parasitic capacitance induced by the AFM probe's cone, and the presence of a water meniscus at the tip-sample interface.

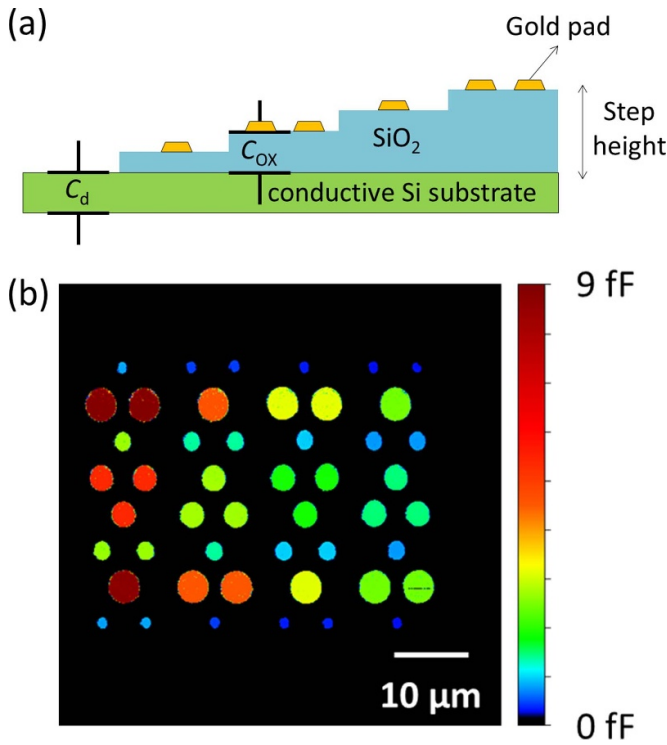


Figure 2. (a) Schematic side view of the standard sample. (b) Capacitance map obtained on MC2 capacitive standard with the calibrated SMM [4].

2.2. Calibration sample

The SMM measurements have been experimentally calibrated using a commercial capacitance calibration standard (MC2 Technologies, France), as shown in figure 2. The capacitance standard comprises 144 patterns, each one includes 48 micrometer-sized metal–oxide semiconductor (MOS) capacitors, with capacitance values ranging from 0.3 fF to 9.2 fF [3].

This calibration kit was fully characterized through traceable capacitance measurements with uncertainty below 3% using a SMM (5600LS from Keysight, USA) under a nitrogen atmosphere inside a glove box (MBraun, Germany). The thicknesses (h_{SiO_2}) of the dielectric terrace-like layers were measured by a metrologically-characterized AFM system (Nanoman V model, Veeco, USA), using a silicon tip with an apex radius below 10 nm (OTESPA-R3, Bruker, USA). The AFM system was dimensionally calibrated using a surface topography standard (P900H60, LNE-C2N, France) [10]. The gold pads' areas were evaluated using scanning electron microscopy and AFM images.

Using dimensional data with the nominal dielectric constant of SiO_2 ($\epsilon_r = 3.9$) [11], we computed the capacitance of each MOS capacitor using the parallel plate capacitor formula

$$C = \epsilon_0 \epsilon_{r, \text{SiO}_2} \frac{A}{h_{\text{SiO}_2}}, \quad (3)$$

where ϵ_0 is the electrical permittivity of the vacuum. However, as the area of the top electrical contact (i.e. gold pad radius) becomes smaller compared to the thickness of the dielectric layer, fringing fields become more dominant in the capacitance value and equation (3) is no longer accurate [12]. Consequently, it proves highly advantageous to use finite element modeling to compute true capacitance values.

3. Capacitance determination

Although direct impedance measurements are possible at sub-micrometric resolution by measuring the potential to electric current ratio (I – V method) with an AFM tip [13], this technique can only operate at low frequency (10 kHz). Two types of measurement setups exist to evaluate impedance in RF and MW domain [14]. The RF I – V method measures the potential to electrical current ratio and requires the test impedance to be included in the transmission line which is not possible for the sample considered. The other option is to perform a calibrated S_{11} measurement. This requires an impedance standard with impedance computed from device dimensions. The sample on which this paper is based was fully characterized in previous work [4].

We performed numerical simulations to compute the capacitance C associated with each capacitive structure, considering the fringing field contributions. To this end, Poisson's equation was solved by using Comsol Multiphysics 5.6 with the AC/DC module,

$$\nabla^2 V = -\frac{\rho}{\epsilon_0 \epsilon_r} \quad (4)$$

where ρ is the charge density, and V is the electrical potential. Figure 3 illustrates the 2D axisymmetric electromagnetic model and the implemented simulation box. A 1 V potential was applied to the top electrical contact (green dashed line) while the back electrode (violet dashed line) was set to 0 V. We used the MUMPS solver [15] with a maximal element size of 20 nm.

Once the solution is computed in this configuration, we calculate the capacitance of the structure using equation (5) over the back electrode:

$$C = \frac{\iint_{\text{back electrode}} \vec{D} \cdot d\vec{s}}{\Delta V}, \quad (5)$$

where D is the displacement field and ΔV is the voltage difference between the top and bottom electrodes. In [4], we used the results of this simulation to calibrate the SMM on the reference standard with a 3% uncertainty level.

To verify that the solution is independent of the FEM solver, we used FEniCS, a model based on the open source Python library for FEM [16]. The mesh was obtained by GMSH [17]. The solution to Poisson's equation was computed by a sparse lower–upper solver. The results obtained with FEniCS agree with those obtained in Comsol simulations within 0.1%.

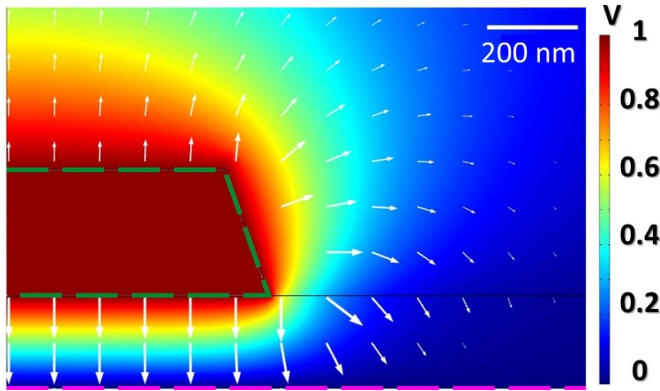


Figure 3. Solution to Poisson's equation for a gold pad of radius 500 nm and thickness 277 nm on a SiO₂ layer of 200 nm. The color map represents the electrical potential distribution, where the white arrows correspond to the electric field lines. The arrow length is represented on a 20 log base of the field norm with a scale factor of $1.5 \cdot 10^{-5}$.

4. RF model

Once the capacitance of the reference standard is determined via FEM, we simulate the wave propagation in the SMM setup to evaluate the impact of stray impedances on the calibration procedure. These simulations are performed by Comsol Multiphysics 5.6 with the RF module.

4.1. Simulation box description

4.1.1. Geometry of the simulation box. The simulation box comprises an AFM tip on top of a MOS capacitor. We consider the nominal geometry of the Rocky Mountain Nanotechnology (RMN, USA) probe, which is commonly used in our experimental measurements. The cone height (h_1) is set to 80 μm , the apex radius (r) is set at 80 nm, and the radius of contact (ξ) is set at 48 nm. We position the AFM tip at the center of the simulation box to exploit the rotational symmetry.

The MW signal is injected through a coaxial port at the top of the simulation box. The beginning of the AFM probe's cone is pushed away from the port by a straight section of length h_2 . This length is set to avoid any reflection from the straight to the conical transition [18]. Finally, a perfect electric conductor (PEC) boundary condition is set on the right and bottom edges of the simulation box. The MW signal is injected at the red continuous line, and propagated by the coaxial waveguide formed between the AFM tip and the right PEC boundary condition.

4.1.2. Equation to be solved. Our objective is to solve the wave propagation equation directed by the SMM tip. The general wave propagation equation is given by equation (6),

$$\vec{\nabla} \times \mu_r^{-1} (\vec{\nabla} \times \vec{E}) - k_0^2 \left(\epsilon_r - \frac{j\sigma}{\omega\epsilon_0} \right) \vec{E} = \vec{0}, \quad (6)$$

where μ_r is the relative magnetic permeability, \vec{E} is the electric field, k_0 is the wave vector, and ω is the angular frequency. The port condition to inject the MW signal in the simulation box is given by equation (7),

$$\hat{n} \times (\vec{\nabla} \times \vec{E}) + jk_0 \hat{n} \times (\vec{n} \times \vec{E}) = \vec{0}, \quad (7)$$

where \hat{n} is the normal element. The propagation mode in the coaxial waveguide is transverse electromagnetic, where both the electric and magnetic fields are normal to the propagation direction. In our SMM experiments, the AFM tip is made of platinum, and the top electrical pad is made of gold. The 0.120 V surface potential difference between those two materials [19] was not taken into account for simplicity matter. Nevertheless, in the simulations, the AFM tip and top electrical contact material was set to gold with a high electrical conductivity ($0.456 \cdot 10^{12} \text{ S m}^{-1}$), resulting in a skin depth of 1.4 nm for an excitation frequency of 300 GHz.

The capacitance (C_z) of the structure was obtained from the potential to current ratio (i.e. complex impedance), where the current I is given by evaluating equation (8) at the red cross in figure 4(a),

$$I = \oint \vec{B} \cdot d\vec{l}, \quad (8)$$

where \vec{B} is the magnetic field. The voltage is given by equation (9) evaluated over the green dashed line in figure 4(a)

$$\Delta V = \int \vec{E} \cdot d\vec{s}, \quad (9)$$

where \vec{E} is the electric field. Note that here the depletion capacitance of the MOS structure is not taken into account but in practice it is taken into account, see [4]. The S_{11} parameter is evaluated at the port condition by equation (1),

$$S_{11} = \frac{\int_{\text{Port1}} \left((\vec{E}_C - \vec{E}_1) \cdot \vec{E}_1^* \right) dA_1}{\int_{\text{Port1}} \left(\vec{E}_1 \cdot \vec{E}_1^* \right) dA_1} \quad (10)$$

where \vec{A}_1 is the normal element to the port boundary, \vec{E}_C is the electric field computed at the port condition and \vec{E}_1 is the electric field pattern of the eigenmodes at the port 1. An eigenmode analysis was performed for the specific port 1 before solving the Maxwell's equations by Comsol to know \vec{E}_1 [20].

Finally, the frequency of the MW signal must be chosen. Typically, our experiments run in the frequency range between 0.5 GHz and 20 GHz, corresponding to a wavelength of 14 mm. To properly mesh the apex of the probe, the mesh size in this region was set below 1 nm. This leads to a low-frequency breakdown problem [21]. To solve this issue, we worked with a higher excitation frequency (300 GHz) corresponding to a wavelength of 1 mm.

The electric properties of the dielectric layer, water meniscus, and conductive part (AFM tip and top electrode) were

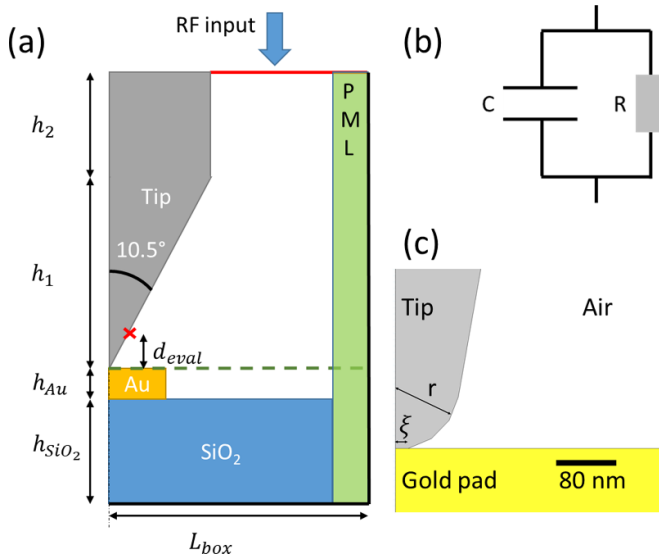


Figure 4. (a) Simulation box configuration (not to scale). Green dashed line: control integral for potential evaluation; red cross: control point for current evaluation; green rectangle: perfectly matched layer (PML); Bold black boundary line: perfect electric conductor (PEC). (b) Lumped elements model. (c) Zoom on the tip apex.

Table 1. Relative difference between the capacitance computed at 20 GHz and 300 GHz.

C_z (fF)	ΔC_z (%)	$\Delta C_{S_{11}}$ (%)
0.24	3.65	3.65
9.36	3.51	3.51

set at their 20 GHz values. Additional computations were performed with Comsol Multiphysics 6.0 with frequency of 20 GHz with little change in the capacitance value (C_z and $C_{S_{11}}$). The table 1 reports the relative deviation in C_z and $C_{S_{11}}$ at 20 GHz and 300 GHz.

4.1.3. Meshing and perfectly matched layer (PML) boundary condition. In the absence of the PML, the right edge of the boundary box creates an artificial wave reflection irrelevant in actual SMM experiments. This phenomenon is manifested by the dependence of the complex voltage drop, complex current, and complex capacitance on the d_{eval} parameter, as shown in figure 5(a). The simplest way to mitigate this issue is to extend the simulation box to the right. Typically, the lateral size of the free space surrounding the capacitor should be at least a few wavelengths large [20]. The small apex size (below 50 nm) imposes a very small meshing element (0.5 nm mesh size) in this region, as mentioned before. The computation cost of a simulation using this mesh size would be prohibitive. Thus, we opted for an adaptive meshing size, with a large element far from the AFM tip. To limit the computation error, we take the conservative choice of having a transfinite line over the top electrical contact with a 1 nm mesh size,

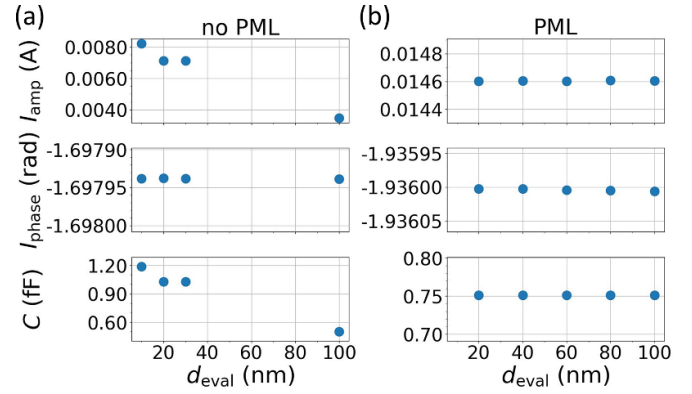


Figure 5. Evaluation of the amplitude and phase of the electric current flowing in the tip and the capacitance of the structure as a function of the current evaluation distance in the case of (a) no PML implemented, and (b) PML implemented.

and another line over the apex of the probe with a 0.5 nm mesh size. Moreover, to avoid any discontinuity, the growth of these elements, i.e. the change in size between two adjacent elements, has been limited to limited to a 1.1 factor. However, since the computation cost of meshing the simulation box of 5-wavelength length is out of our system's reach, we chose to implement a PML [22] at the interface between the free space region and the PEC right boundary condition. This PML acts as an absorbing region that attenuates the reflection of the MW signal.

The impact of the PML on the simulation is shown in figure 5(b), where the capacitance of the structure is noticeably independent of d_{eval} , similar to the SMM experiments. Those data were obtained with an L_{box} of 60 μm (i.e. 3/50 of the wavelength), corresponding to a reasonable computation time.

4.2. Self-calibration of the simulation

We conducted a series of simulations by varying the gold pad radius and the dielectric layer thickness to cover the whole range of capacitances in the reference sample used in SMM experiments. The S_{11} parameter evaluated at the port condition differs from the one estimated at the tip-sample interface due to the impedance of the SMM tip [23]. The calibration was done using three reference capacitances (C_z). Figure 6(a) shows the relative deviation between the reference and calibrated capacitances.

The capacitances used to compute the error parameters in equation 2 are encircled in blue. The relative deviation is below 0.8% for all capacitances, and below $4 \cdot 10^{-12}$ for the three capacitances used as references. The Smith chart of the raw (blue point) and calibrated (green points) S_{11} is shown in figure 6(b). The capacitance values used for the calibration are located at the intersection of the iso-resistive and iso-capacitive circles (dashed line). We notice that the S_{11} parameter is associated with a null resistance after calibration, which is

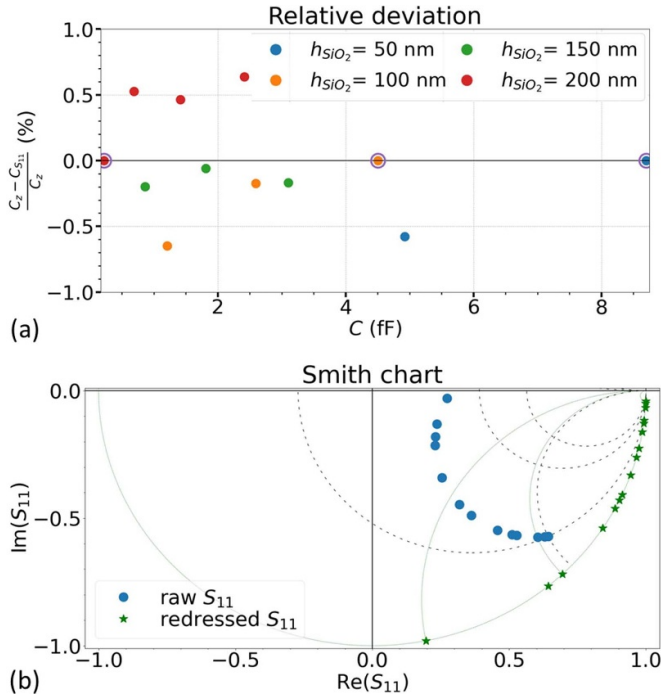


Figure 6. Self-calibration of a tip on top of a capacitive MOS structure. (a) Relative deviation between the capacitance estimated at the calibrated reference plane (C_z) and the capacitance (C_{S11}). (b) Smith chart, where the impedances used for the calibration are marked by dashed lines.

expected as the simulated calibration device is set with a perfect dielectric.

5. Water meniscus implementation

A water meniscus is formed at the interface between the tip apex and the sample surface. Several groups have investigated the formation [24, 25], shape [24, 26, 27], and impact of the water meniscus on electrical measurements [19, 28]. The expected parasitic capacitance from the water meniscus is in the range of a few aF. Our goal is to investigate the impact of the sole water meniscus on the impedance calibration in SMM.

5.1. Water meniscus geometry

The geometry of the implemented water meniscus is extracted from [25], as shown in figure 7.

Here, R is the apex's radius, ψ is the fill angle, θ_1 and θ_2 are the contact angle at the Pt tip and at the Au pad, respectively, and r_1 defines the water meniscus. The relative dielectric of the water meniscus was set to 10 and its conductivity was let at its default value of $5.5 \mu\text{S m}^{-1}$. The geometry depends on the volume of the water meniscus and the angle of contact between platinum (at the apex surface) and gold (at the sample's electrode). Numerically, the shape of the water meniscus is defined by the thickness of the absorbed water layer and the r_1 parameter.

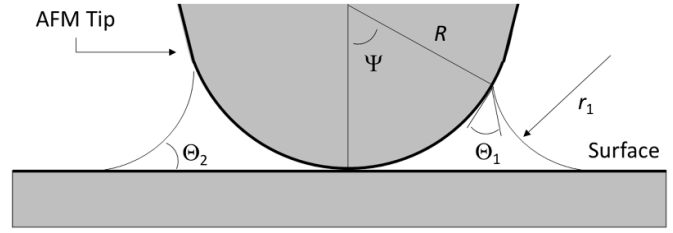


Figure 7. Water meniscus at the tip apex-sample interface model. Reproduced with permission from [25].

5.2. Comparison with experimental data

The relationship between the adhesion force of an AFM tip retracted from a planar surface, and the geometrical properties of the water meniscus is given by [27]

$$F_{\text{adh}} = F_{\text{stv}} + \frac{F_t + F_p}{1 + e^{\frac{\text{RH} - \text{RH}'}{m}}} \quad (11a)$$

$$F_t = 2\pi \gamma_w R \sin(\psi) \sin(\psi + \theta_1) \quad (11b)$$

$$F_p = -2\pi \gamma_w R^2 \sin(\psi)^2 H(\theta_1, \theta_2, \psi). \quad (11c)$$

F_{adh} is the adhesion force, F_{stv} is the contribution from vapor water, F_t and F_p are the contributions to the capillary force due to the surface tension and pressure difference, respectively. γ_w is the surface tension of water set at $72 \text{ mN}\cdot\text{m}^{-1}$ [29], RH and RH' are the relative humidities of the current experiment and the transition from ice-like to bulk water behavior, respectively, where m is the slope of this transition, as defined in [27]. ψ is the filling angle, θ_1 and θ_2 are the contact angles at the tip and sample surface, respectively. H is the local mean curvature of the meniscus, as defined in [30]. A scan over a tip characterizer sample (Supracon, Germany) was acquired with a contact force of $35 \text{ nN} \pm 15 \text{ nN}$ to extract the apex radius [31]. The obtained tip radius is $289 \text{ nm} \pm 14 \text{ nm}$, which is large compared to the nominal value of 20 nm . This significant deviation can be explained by the large number of scans acquired with the used AFM tip prior to the measurement campaign. It has been done with the purpose of reducing the uncertainty on the apex radius by increasing its absolute value. A series of approach retract curves above a gold surface were recorded at different humidity levels using a platinum tip (12Pt300A, RMN, USA), with a nominal spring constant of $0.8 \text{ N m}^{-1} \pm 0.3 \text{ N m}^{-1}$. The variations in the adhesion force as a function of the relative humidity are reported in figure 8. The relative humidity was modified by opening the large load lock of the glove box for a controlled time, and homogenized by circulating nitrogen inside the glove box. The RH was monitored near the scanning region using a ppm H_2O sensor.

The RH' and transition slope values were extracted from the data shown in figure 8. Knowing the apex radius and the contact angles of a water drop on Ti ($\theta_1 = 32^\circ$, [32]) and Au surface ($\theta_2 = 40^\circ$, [33]), we were able to compute a filling angle of $11^\circ \pm 2^\circ$ associated with the meniscus. This filling

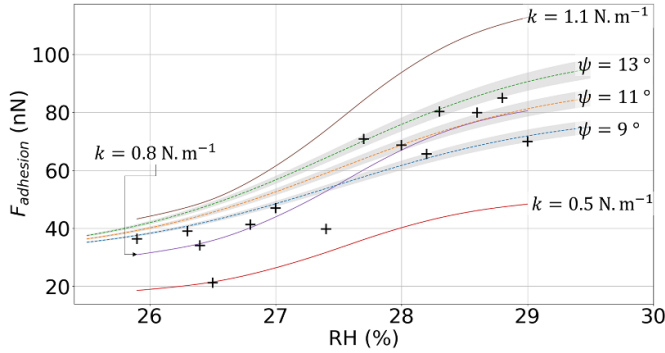


Figure 8. Evolution of the adhesion force as a function of the relative humidity. Black cross: experimental values. SOLID Line: fit of experimental data. Dashed line: adhesion model (from [27]) with uncertainty associated to the apex radius.

angle has been implemented in the simulation data shown in figure 8. Maps of the S_{11} over the reference capacitive standard (A64, MC2 Technologies, France) were acquired at the different RH levels using the same AFM tip.

5.3. Impact of the water meniscus on the mSOL calibration

A water meniscus with an absorbed layer thickness of 1 nm and a filling angle of 15° was implemented at the tip-sample's interface. The relative dielectric constant of water was set to $\epsilon_r = 10$ (lower than that of bulk water according to [34]) due to the small size of the absorbed layer and the meniscus. The impact of this meniscus on the wave propagation and the calibration is shown in figure 9, where the \log_{10} of the electric field and the electric field vector inside the water meniscus are shown in (a). In this particular example, the SMM tip was located on top of a gold pad of radius 500 nm on a 50 nm SiO_2 terrace. Figure 9(b) shows the relative deviation between the calibrated capacitance ($C_{S_{11}}$) without and with water meniscus attached to the apex of the tip. The calibration was done only in absence of the water meniscus. The obtained parameters were then applied to both configurations. The presence of water meniscus results in a deviation in the calibrated capacitance up to 0.3%. This value is in good agreement with previous experimental data [4] where SMM scans were performed at different RH values. The estimated water meniscus contribution was then estimated at the 0.2% level. It should be noted that, in reality, calibration and measurement are done with a water meniscus present. Thus, observable discrepancies due to the water meniscus between measured value and calibrated value are even smaller.

The electrical properties of the water meniscus can undergo large changes with dielectric constant ranging from 2 to 80 and electrical conductivity ranging from a few 10^{-6} S m^{-1} to a few tenths of S m^{-1} . As before the calibration was performed in the configuration without water meniscus, then the electrical properties were changed within the realm of possible. The relative deviation between the capacitor from calibrated S_{11} in the two configurations (with and without water meniscus) is shown in figure 10.

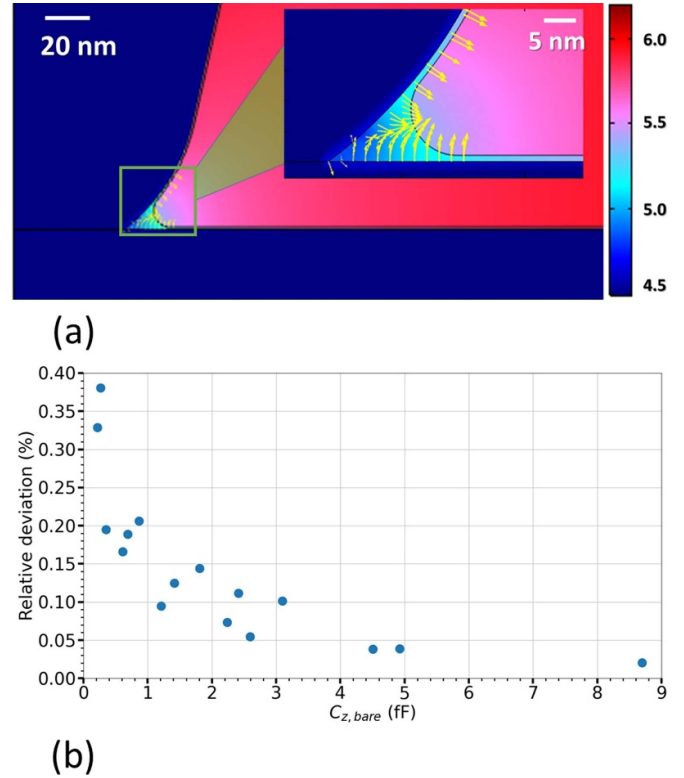


Figure 9. (a) $\log_{10} |\vec{E}|$ at the tip-sample interface for a water meniscus ($h = 1 \text{ nm}$; $r_1 = 20 \text{ nm}$), inset zoom at the water meniscus. (b) Relative deviation between C_z (without water meniscus) and $C_{S_{11}}$ calibrated with the error parameters obtained with a bare tip applied to a tip with a water meniscus.

Computation performed on the smallest capacitor,
 $f_{VNA} = 300 \text{ GHz}$

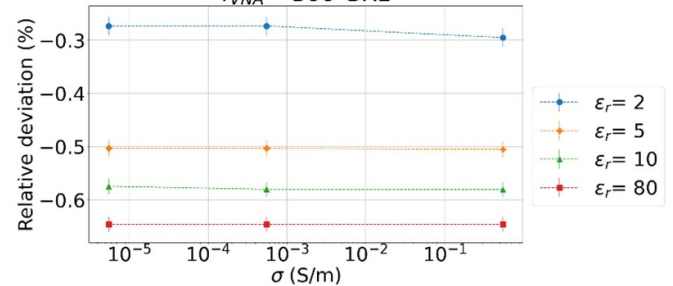


Figure 10. Relative deviation between the smallest capacitance with and without water meniscus as a function of the electrical properties of the water meniscus. The error parameters for the calibration were obtained in the configuration without water meniscus.

The absolute value of the relative deviation increases with the dielectric constant of the water meniscus while its electrical conductivity seems to have no effect. It is an expected result as the water's electrical conductivity is much lower than the one of the gold pad ($0.456 \cdot 10^{12} \text{ S m}^{-1}$).

6. Summary and outlook

In this paper, we presented the development of a digital-twin environment to investigate the effects of experimental and

environmental parameters on SMM measurements. We simulated the self-calibration method for capacitance measurement by SMM with a maximal deviation of $\pm 0.8\%$ relative to reference capacitances determined via electrostatic calculations. Furthermore, we implemented a water meniscus at the tip-sample interface to assess its impact on SMM measurements. Our results showed a 0.4% relative deviation on the calibrated capacitance, which is coherent with previous experimental data. These results were compared to experimental measurements to determine the shape of the water meniscus. Our proposed numerical environment offers means to further investigate parasitic factors to SMM measurements. It is expected to facilitate future improvements of electromagnetic measurement accuracy at the nanoscale.

Future work would include the study of the impact of non conductive material at the tip sample interface to simulate the impact of resist remaining that can be observed in SMM experiment over such calibration structure. An attention could also be drawn to the impact of rough surface.

Data availability statement

All data that support the findings of this study are included within the article (and any supplementary files).

Acknowledgment

This research work was carried out in the framework of the ELENA project (EMPIR 20IND12), which is supported by the European Metrology Programme for Innovation and Research (EMPIR). The EMPIR initiative is co-funded by the European Horizon 2020 research and innovation program and the EMPIR Participating States.

ORCID iDs

Damien Richert  <https://orcid.org/0009-0006-3293-4352>
François Piquemal  <https://orcid.org/0000-0002-7950-0475>

References

- [1] Gramse G, Kasper M, Fumagali L, Hinterdorfer P and Kienberger F 2014 Calibrated complex impedance and permittivity measurements with scanning microwave microscopy *Nanotechnology* **25** 145703
- [2] Tuca S S, Badino G, Gramse G, Brinciotti E, Kasper M, Oh Y J, Zhu R, Rankl C, Hinterdorfer P and Kienberger F 2016 Calibrated complex impedance of CHO cells and E. coli bacteria at GHz frequencies using scanning microwave microscopy *Nanotechnology* **27** 135702
- [3] Dunsmore J P 2012 *Handbook of Microwave Component Measurements: With Advanced VNA Techniques* (Wiley)
- [4] Piquemal F, Morán-Meza J, Delvallée A, Richert D and Kaja K 2021 Progress in traceable nanoscale capacitance measurements using scanning microwave microscopy *Nanomaterials* **11** 820
- [5] Richert D, Morán-Meza J, Kaja K, Delvallée A, Allal D, Gautier B and Piquemal F 2021 Traceable nanoscale measurements of high dielectric constant by scanning microwave microscopy *Nanomaterials* **11** 3104
- [6] Gungor A C, Celuch M, Smajic J, Olszewska-Placha M and Leuthold J 2020 Electromagnetic and semiconductor modeling of scanning microwave microscopy setups *IEEE J. Multiscale Multiphysics Comput. Tech.* **5** 209–16
- [7] Olszewska-Placha M, Celuch M, Le Quang T, Gungor A C, Hoffmann J, Smajic J and Rudnicki J. 2020 Open access CAD, em tools, and examples for teaching microwaves. *2020 23rd Int. Microw. Radar Conf. MIKON 2020* pp 402–6
- [8] Richert D, Kaja K, Mor J A, Gautier B, Deleruyelle D and Piquemal F 2023 A fully-numerical environment for evaluating the robustness of the short open load calibration for capacitance measurements in scanning microwave microscopy 108–10
- [9] Brinciotti E et al 2015 Probing resistivity and doping concentration of semiconductors at the nanoscale using scanning microwave microscopy *Nanoscale* **7** 14715–22
- [10] Crouzier L, Delvallée A, Ducourtieux S, Devoille L, Noircler G, Ulysse C, Taché O, Barluet E, Tromas C and Feltin N 2019 Development of a new hybrid approach combining AFM and SEM for the nanoparticle dimensional metrology *Beilstein J. Nanotechnol.* **10** 1523–36
- [11] Janezic M D, Arz' U, Begley S and Bartley P 2009 Improved permittivity measurement of dielectric substrates by use of the TE111 mode of a split-cylinder cavity *73rd ARFTG Microw. Meas. Conf. Spring 2009—Pract. Appl. Nonlinear Meas* pp 1–3
- [12] Sloggett G J, Barton N G and Spencer S J 1986 Fringing fields in disc capacitors *J. Phys. A: Math. Gen.* **19** 2725–36
- [13] Estevez I, Chrétien P, Schneegans O and Houzé F 2014 Specific methodology for capacitance imaging by atomic force microscopy: a breakthrough towards an elimination of parasitic effects *Appl. Phys. Lett.* **104** 083108
- [14] Keysight Technologies 2009 *Impedance Measurement Handbook (Agilent)* p 140
- [15] Amestoy P R, Buttari A, L'Excellent J-Y and Mary T 2019 Performance and scalability of the block low-rank multifrontal factorization on multicore architectures *ACM Trans. Math. Softw.* **45** 1–26
- [16] Logg A, Mardal K A and Wells G 2012 *Automated Solution of Differential Equations by the Finite Element Method: the FEniCS Book vol 84*
- [17] Geuzaine C and Remacle J F 2009 Gmsh: a 3-D finite element mesh generator with built-in pre- and post-processing facilities *Int. J. Numer. Methods Eng.* **79** 1309–31
- [18] Issa N A and Guckenberger R 2007 Optical nanofocusing on tapered metallic waveguides *Plasmonics* **2** 31–37
- [19] Mugo S and Yuan J 2012 Influence of surface adsorption on work function measurements on gold-platinum interface using scanning kelvin probe microscopy influence of surface adsorption on work function measurements on gold-platinum interface using scanning kelvin probe microscopy *J. Phys.: Conf. Ser.* **371** 012030
- [20] Comsol 2017. *RF module user's guide*
- [21] Wu B Y, Sheng X Q, Fabregas R and Hao Y 2017 Full-wave modeling of broadband near field scanning microwave microscopy *Sci. Rep.* **7** 1–8
- [22] Johnson S G 2021 Notes on perfectly matched layers (PMLs) (arXiv: 2108.05348v1)
- [23] Azizi M 2017 CMOS-MEMS scanning microwave microscopy
- [24] Wei Z and Zhao Y P 2007 Growth of liquid bridge in AFM *J. Phys. D: Appl. Phys.* **40** 4368–75
- [25] Charlaix E and Ciccotti M 2020 Capillary condensation in confined media pp 219–36

- [26] Assy A, Lefèvre S, Chapuis P-O and Gomès S 2014 Analysis of heat transfer in the water meniscus at the tip-sample contact in scanning thermal microscopy *J. Phys. D: Appl. Phys.* **47** 442001
- [27] Sedin D L and Rowlen K L 2000 Adhesion forces measured by atomic force microscopy in humid air *Anal. Chem.* **72** 2183–9
- [28] Wang F, Clément N, Ducatteau D, Troadec D, Tanbakuchi H, Legrand B, Dambrine G and Théron D 2014 Quantitative impedance characterization of sub-10 nm scale capacitors and tunnel junctions with an interferometric scanning microwave microscope *Nanotechnology* **25** 405703
- [29] Vargaftik N B, Volkov B N and Voljak L D 1983 International tables of the surface tension of water *J. Phys. Chem. Ref. Data* **12** 817–20
- [30] Orr F M, Scriven L E and Rivas A P 1975 Pendular rings between solids: meniscus properties and capillary force *J. Fluid Mech.* **67** 723–42
- [31] Kwak G Y, Chang H J, Na M Y, Ryu S K, Kim T G, Woo J C and Kim K J 2021 Calibration of high magnification in the measurement of critical dimension by AFM and SEM *Appl. Surf. Sci.* **565** 150481
- [32] Li Z, Beck P, Ohlberg D A A, Stewart D R and Williams R S 2003 Surface properties of platinum thin films as a function of plasma treatment conditions *Surf. Sci.* **529** 410–8
- [33] Nguyen C T, Barisik M and Kim B 2018 Wetting of chemically heterogeneous striped surfaces: molecular dynamics simulations *AIP Adv.* **8** 065003
- [34] Fumagalli L *et al* 2018 Anomalously low dielectric constant of confined water *Science* **360** 1339–42